COVARIANCE INTERSECTION–BASED SENSOR FUSION WITH LOCAL MULTIPLE MODEL HYPOTHESIS TESTING FOR SOUNDING ROCKET TRACKING AND IMPACT POINT PREDICTION

Julio Cesar Bolzani de Campos Ferreira
Embraer - Empresa Brasileira de Aeronáutica - 12227-901 - São José dos Campos - SP - Brazil
julio.ferreira@embraer.com.br

Jacques Waldmann
Instituto Tecnológico de Aeronáutica - CTA-ITA-IEES - 12228-900 - São José dos Campos - SP - Brasil
jacques@ita.br

Abstract. *The estimation of position, velocity, and acceleration of a moving object based on radar measurements is critical for air traffic control, airborne surveillance systems, orbital vehicles launching and impact point prediction. This paper investigates covariance intersection (CI) for fusion of actual data from a pair of distinct radar sites at the Alcântara Launch Center (ALC) for the tracking of sounding rockets and impact point prediction to comply with safety-of-flight issues. De-biased measurement transformation from spherical to cartesian coordinates and multiple model hypotheses testing are employed in the local processing node at each radar site. Boost and free fall models are embedded in a Kalman filter to produce local estimates of position, velocity, and acceleration. The local estimates and corresponding covariance matrices from the radar sites are transformed to the common reference frame at the launch-pad and CI-fused. All simulations presented herein make use of actual radar data of a VS30 sounding rocket launch that occurred at ALC in February, 2000. Impact point prediction considers uncertainties inferred from the computed covariance matrix, culminating in an ellipsoidal impact area with a given impact probability. The results of the fusion approach present a much improved performance over the present procedure in ALC for trajectory tracking and impact point prediction for sounding rocket payload recovery.*

Keywords*: Sounding rockets, radar tracking, sensor fusion, Kalman filter, impact point prediction.*

1. Introduction

Accurate impact point determination and successful payload orbital injection are the major motivations in this investigation of sensor fusion. The former has a fundamental role in safety-of-flight issues when launching sounding rockets into space (Wertz, 1978). The mission control crew must be aware of a critical failure to abort the launch phase and command the destruction of the vehicle. The decision is based on impact point estimation, whose accuracy strongly relies on the quality of vehicle position and velocity estimates. Regarding payload orbital injection, it demands accurate estimation of position and velocity for the adequate prediction of orbit parameters that enables ground stations to track and send command signals for proper satellite positioning and the opening of solar panels to allow the replenishing of the on–board batteries. Poor estimates of orbit parameters may lead to a catastrophic inability to track and send commands to the satellite, hence causing its loss. Thus, safety-of-flight requirements and the need to severely limit the probability of a critical failure dictate the need for redundancy at various levels. Additionally, a trend towards improving tracking reliability and accuracy has been to complement radar data from distinct sites on the ground with inertial and GPS measurements acquired on board the vehicle and transmitted to mission control via telemetry in real time (Montenbruck *et al.*, 2002). Along with sensor redundancy, the effective use of qualitatively distinct data calls for an appropriate sensor fusion strategy.

Sensor fusion is a framework that comprises means and tools for the alliance of data originating from different sources. The complexity of the fusion approach described here lies in performing data alignment, tracking, and finding relationships between objects and observed events. The latter corresponds to the classification of the flight phase into boost or free fall. Covariance intersection (CI) (Peters, 2001; Uhlmann, Csorba, Julier, and Durrant-Whyte, 1997) and track-to-track (Bar-Shalom and Li, 1993; Brookner, 1998) are fusion methods often used for target tracking from local estimates. Both process radar data locally with a Kalman filter, which provides a measure of its estimation accuracy. That is a valuable feature for impact point prediction and corresponding area uncertainty.

The use of actual launch data is a much significant contribution, and yields a more realistic development and assessment of filtering and fusion techniques in comparison with the use of simulated data by anticipating important practical issues. The actual data was acquired from ALC radars in February, 6th, 2000 during the launch operations of a VS30, single–stage sounding rocket.

Section 2 presents the Kalman-filter formulation of boost and free-fall flight models for locally estimating sounding rocket position, velocity, and acceleration. Section 3 describes the multiple hypothesis testing (MHT) used to locally weigh both flight models to yield the local-level estimates. Section 4 presents the CI–based fusion of local-level estimates, whereas Section 5 describes the use of the fused estimates and their respective uncertainties for predicting the impact point and its surrounding area of uncertainty with a given impact probability. Section 6 shows results concerning

local-level MHT estimation, CI-based fusion, impact point prediction and impact uncertainty area, and section 7 presents the conclusions.

2. Local–level Kalman filter estimation

Radars naturally provide measurements in spherical coordinates. Tracking yields a nonlinear process model when measurements are in spherical coordinates, whereas the measurement model is nonlinear in cartesian coordinates. The use of cartesian coordinates is quite appropriate to accomplish the necessary transformations of local radar data to a common coordinate frame. However, unbiased errors in spherical measurements turn into biased errors in cartesian measurements. Hence, the resulting transformed data is unsuitable for optimal estimation under the assumption of unbiased measurement errors. Instead of resorting to a nonlinear filtering approach, East–North–Up (ENU) cartesian coordinates are used with a de-biased conversion method (Lerro and Bar-Shalom, 1993). At each radar site, the measurements in spherical coordinates are converted into de-biased cartesian coordinates that feed the local Kalman filter. Assuming unbiased, mutually uncorrelated, Gaussian radar measurement noise in spherical coordinates, the de-biased cartesian coordinates are given by Eq. (1) where r, α, and θ are the spherical coordinates slant range, elevation, and bearing, respectively (Peters, 2001):

$$\begin{bmatrix} x \\ y \\ z \end{bmatrix} = \begin{bmatrix} rc\alpha c\theta(1-\exp(-\sigma_\alpha^2-\sigma_\theta^2)+\exp(-(\sigma_\alpha^2+\sigma_\theta^2)/2)) \\ rc\alpha s\theta(1-\exp(-\sigma_\alpha^2-\sigma_\theta^2)+\exp(-(\sigma_\alpha^2+\sigma_\theta^2)/2)) \\ rs\alpha(1-\exp(-\sigma_\alpha^2)+\exp(-\sigma_\alpha^2/2)) \end{bmatrix} \tag{1}$$

The error variances $\sigma_\alpha^2, \sigma_\theta^2$ are assumed to be constant during radar operation. σ_r^2 is affected by signal-to-noise ratio and target distance. The diagonal measurement noise covariance matrix in spherical coordinates $\mathbf{R_{radar,s}}$ is seen in Eq. (2), where β is the inverse of the radar pulse width, *SNR* is the monitored signal-to-noise ratio, and r is the slant range to target in meters. σ^2_{cte} is a constant term and c_0 is the speed of light in m/s.

$$\mathbf{R_{radar,s}} = \mathrm{diag}\left(\sigma_\alpha^2 \quad \sigma_\theta^2 \quad \sigma_{cte}^2 + \left(\frac{c_0}{2\beta\sqrt{SNR}} \right)^2 + (50.10^{-6} r)^2 \right) \tag{2}$$

After the de-biased transformation, the resulting measurement noise covariance matrix $\mathbf{R_{radar,c}}$ in cartesian coordinates, with nonzero off-diagonal terms indicating spatially correlated measurement errors can be found in Peters (2001). Simulation showed that the off-diagonal terms become relevant as the vehicle progresses along its trajectory. That spatial correlation motivates a target kinematics model with a state transition matrix $\mathbf{\Phi}$ comprising all three directions. The measurement vector $\mathbf{y}$ representing the vehicle position in local NED coordinates is:

$$\mathbf{y}(k) = \mathbf{H}\mathbf{x}(k) + \mathbf{v}(k) \qquad \mathbf{H} = \begin{bmatrix} 1 & & 0 & & 0 & \\ 0 & \mathbf{0_{3x2}} & 1 & \mathbf{0_{3x2}} & 0 & \mathbf{0_{3x2}} \\ 0 & & 0 & & 1 & \end{bmatrix} \qquad E\{\mathbf{v}(k)\mathbf{v}(j)^T\} = \mathbf{R_{radar,c}}\delta(k-j) \tag{3}$$

When conducting the fusion process, both radars must have their measurements represented in a reference frame. Filtered position and estimated velocities, accelerations, and the corresponding estimation error covariance matrix need to be transformed to the reference frame. The ENU coordinate frame with its origin at the launch-pad is the reference frame. The transformation to the reference frame consists of a rotation, and a translation in the case of position, based on the latitude and longitude coordinates of radar and launch-pad sites. Range, azimuth, and elevation measurements were acquired with a sampling frequency of 1/T=20Hz by both radar facilities located at different sites relative to the launch pad. The VS30 rocket traversed a trajectory consisting of a propulsion phase followed by coasting, the latter characterized by an almost parabolic free fall under the assumption of negligible aerodynamic forces. This assumption is justified by the lack of adequate instrumentation on board the vehicle and on the ground to accurately estimate drag and lift coefficients under realistic launch conditions for use in an aerodynamic model (Farina, 2002; Rogers, 2003). The former employed simulated data, and the latter focussed on off-line reconstruction of a ballute-stabilized payload descending from the upper layers through a rigid model of the atmosphere. The perturbations due to aerodynamic forces are more intense in the dense layers of the atmosphere and are thus confined to the early boost phase and the final descent of the payload. *The reentry phase is characterized by an unstable, tumbling motion which renders accurate modelling extremely difficult for real-time purposes*. Interactions with the atmosphere must, therefore, be considered as perturbations affecting the real-time impact point prediction and adequate tolerances have to be incorporated into safety-of-flight procedures making use of that prediction (Montenbruck *et al.*, 2002). A parachute deploys in the final moments of descent for the safe recovery of the payload.

Singer (1970) described 2-D manned maneuvering targets in range-bearing coordinates. It has been adapted to the VS30 rocket kinematics in 3-D ENU cartesian coordinates in each flight phase along direction *n=x,y,z* at a radar site:

$$\begin{bmatrix} \dot{p}_n(t) \\ \dot{v}_n(t) \\ \dot{a}_n(t) \end{bmatrix} = \mathbf{F}\begin{bmatrix} n(t) \\ v_n(t) \\ a_n(t) \end{bmatrix} + \mathbf{G}w_n \qquad \mathbf{F} = \begin{bmatrix} 0 & 1 & 0 \\ 0 & 0 & 1 \\ 0 & 0 & -\alpha_n \end{bmatrix} \quad \mathbf{G} = \begin{bmatrix} 0 \\ 0 \\ 1 \end{bmatrix} \tag{4}$$

where p_n ,v_n, and a_n are position, velocity, and acceleration, respectively, and w_n is a scalar white process. Parameters $\tau_n = 1/\alpha_n$ is the maneuver correlation time constant, and σ_{an}^2 is the acceleration variance describing maneuver intensity, the latter related in steady state to the white process variance σ_{wn}^2 by satisfying $\sigma_{wn}^2 = 2\alpha_n\sigma_{an}^2$.

Differently from Singer (1970), the model here must cope with acceleration maneuvers with nonzero mean along the vertical direction n=z. The distinct behavior of the propelled and ballistic flight phases calls for multiple models coupled with a multiple hypotheses test (MHT) approach. The launch vehicle experiments a powerful vertical acceleration during the propelled flight phase whereas only gravity is considered afterwards during free fall. One model describes the accelerations in the propelled flight phase whereas another depicts the free fall stage. Empirically tuned, independent probability density functions (p.d.f.) describe the accelerations in the ENU reference frame (x,y pointing north and eastwards, respectively, and z upwards) relative to the radar site. Means and variances of the acceleration processes are computed from the p.d.f.'s shown in Figs. 1-2. The p.d.f. and parameter α_n were tuned so that the Kalman filter yielded a statistically consistent residual. The discrete-time model with state transition matrix $\mathbf{\Phi_n}(\alpha_n, T)$ is:

$$\begin{bmatrix} p_n(k+1) \\ v_n(k+1) \\ a_n(k+1) \end{bmatrix} = \mathbf{\Phi_n}(\alpha_n, T)\begin{bmatrix} p_n(k) \\ v_n(k) \\ a_n(k) \end{bmatrix} + \mathbf{w_{nd}}(k) \qquad \mathbf{\Phi_n}(\alpha_n, T) = \exp(\mathbf{F}T) = \begin{bmatrix} 1 & T & (\alpha_n T - 1 + \exp(-\alpha_n T))/\alpha_n^2 \\ 0 & 1 & (1-\exp(-\alpha_n T))/\alpha_n \\ 0 & 0 & \exp(-\alpha_n T) \end{bmatrix}$$

$$\mathbf{w_{nd}}(k) = \int_{kT}^{(k+1)T} \exp\{\mathbf{F}[(k+1)T - \tau]\}\mathbf{G}w_n d\tau \tag{6}$$

where T is the sample time, $p_n(k)$, $v_n(k)$, and $a_n(k)$ the k-th samples of position, velocity and acceleration estimates along direction n, respectively, and $\mathbf{w_{nd}}(k)$ is a nonzero mean white sequence due to nonzero μ_{az} seen in Figs. 1a)-2a). The fact that vertical acceleration is affected by a nonzero mean white noise sequence should be considered in the target kinematics when implementing the state propagation stage in the Kalman filter. Thus, the deterministic input $\mathbf{u_z}$ (k) caused by $\mathbf{w_{zd}}(k)$ along the vertical is derived. *For the sake of simplicity*, $\mathbf{u_z}$ (k) *is approximated* by considering only the acceleration process nonzero mean:

$$\mathbf{u_z}(k) = E\{\mathbf{w_{zd}}(k)\} = E\{\int_{kT}^{(k+1)T} \exp\{\mathbf{F}[(k+1)T - \tau]\}\mathbf{G}w_z d\tau\} \approx E\{\int_{kT}^{(k+1)T} \begin{bmatrix} 0 \\ 0 \\ \exp\{-\alpha_z[(k+1)T - \tau]\} \end{bmatrix} w_z d\tau\}$$

$$\mathbf{u_z}(k) = \mu_{az}/\alpha_z \begin{bmatrix} 0 & 0 & 1 - \exp\{-\alpha_z T\} \end{bmatrix}^T \tag{7}$$

The propagation of the state estimate $\hat{\mathbf{x}}$ in the Kalman filter is given by:

$$\hat{\mathbf{x}}(k+1|k) = \mathbf{\Phi}\hat{\mathbf{x}}(k|k) + \begin{bmatrix} \mathbf{0_{1x6}} & \mathbf{u_z}^T(k) \end{bmatrix}^T, \quad \hat{\mathbf{x}}(kT) = \begin{bmatrix} p_x & v_x & a_x & p_y & v_y & a_y & p_z & v_z & a_z \end{bmatrix}^T$$

$$\mathbf{\Phi} = \mathrm{diag}(\mathbf{\Phi}_x(\alpha_x, T), \mathbf{\Phi}_y(\alpha_y, T), \mathbf{\Phi}_z(\alpha_z, T)) \tag{8}$$

The estimation error covariance matrix is propagated according to:

$$\mathbf{P}(k+1|k) = \mathbf{\Phi}\mathbf{P}(k|k)\mathbf{\Phi}^T + \mathbf{Q}, \qquad \mathbf{Q} = \mathrm{diag}(\mathbf{Q}_x(\alpha_x, T), \mathbf{Q}_y(\alpha_y, T), \mathbf{Q}_z(\alpha_z, T))$$

$$\mathbf{Q_n}(\alpha_n, T) = E\{(\mathbf{w_{nd}}(k) - E\{\mathbf{w_{nd}}(k)\})(\mathbf{w_{nd}}(k) - E\{\mathbf{w_{nd}}(k)\})^T\}, \ n = x,y,z \tag{9}$$

where the maneuver excitation covariance matrix $\mathbf{Q_n}$ is found in Singer (1970) with parameter σ_{an}^2 according to Figs. 1a and 2a. Along with Eqs. (8)-(9), the remaining update equations of the Kalman filter have been implemented in standard form as follows:

$$\mathbf{K}(k) = \mathbf{P}(k \mid k-1)\mathbf{H}^{\mathbf{T}}(\mathbf{R}_{\mathbf{radar,c}} + \mathbf{H}\mathbf{P}(k \mid k-1)\mathbf{H}^{\mathbf{T}})^{-1}, \quad \hat{\mathbf{x}}(k \mid k) = \hat{\mathbf{x}}(k \mid k-1) + \mathbf{K}(k)(\mathbf{y}(k) - \mathbf{H}\hat{\mathbf{x}}(k \mid k-1))$$

$$\mathbf{P}(k \mid k) = (\mathbf{I} - \mathbf{K}(k)\mathbf{H})\mathbf{P}(k \mid k-1) \tag{10}$$

$\mathbf{P}(0|0)$ demands knowledge of parameters describing the maneuver intensity σ_{an}^2, and sensor noise variance σ_R^2 for each cartesian axis n=x,y,z, which are obtained from the diagonal terms in $\mathbf{R_{radar,c}}$ (Singer, 1970). The initial state $\hat{\mathbf{x}}(0 \mid 0)$ is the distance from each radar site to the launch-pad location, assuming null velocities and accelerations along each cartesian axis despite the occurrence of wind at the launch-pad.

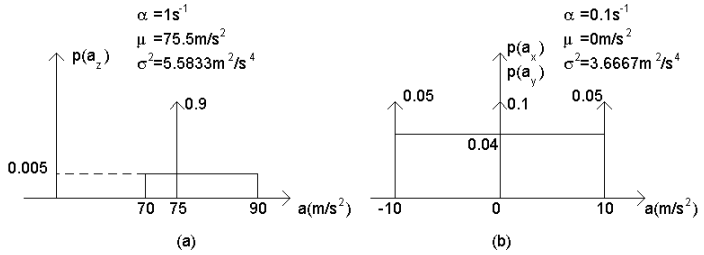

Figure 1 - Acceleration p.d.f. in the propelled flight phase model. a) Vertical. b) Horizontal.

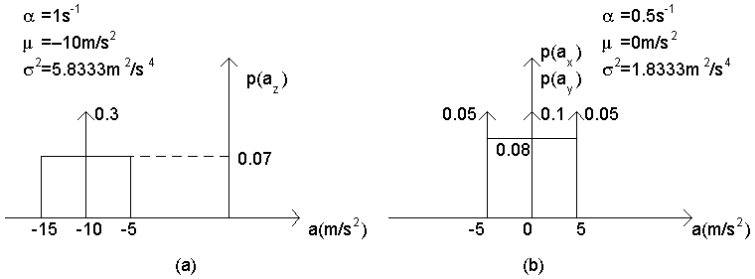

Figure 2 - Acceleration p.d.f. in the free fall phase model. a) Vertical. b) Horizontal.

3. Local-level multiple model hypothesis testing (MHT)

The use of simple models combined with a multiple model approach usually seems more attractive than using a single complex model in terms of modelling and computational efforts (Bak, 2000). The multiple hypothesis testing (MHT) approach evaluates the likelihood of each model and their combination to yield the (sub)optimal estimate (Bar-Shalom and Li, 1993; Willsky *et al.*, 1980). Figure 3 depicts the structure of MHT-based estimation at the local processing node. In what follows, the MHT approach encompasses two distinct local Kalman filters working simultaneously on radar data at the processing node of each radar site, namely Adour and Atlas. Each local filter embeds models M_i i=1,2 of either boost or free fall flight modes, to produce a local, weighed estimate based on the probability that each model is correct. MHT relies on two assumptions: a) the ground-truth is actually described by one of the proposed models, which is the true model, and b) the same true model has been in action since t=0. Then, one hypothesis is formed for each model, namely that the model correctly matches the ground-truth. Assumption a) means that there is no null hypothesis since the true model shall be one from the set of models. The probability that a model M_i is the correct one at time k based on measurements up to $\mathbf{y}(k)$ is:

$$\mu_i(k) \triangleq p(M_i \mid \mathbf{Y_k}) = p(M_i \mid \mathbf{y}(k), \mathbf{Y_{k-1}}) \tag{11}$$

The initial probability $\mu_i(0)$ that model M_i is the correct one is defined by a priori information. From assumption a), all those probabilities sum to unity. The evolution from $\mu_i(k-1)$ to $\mu_i(k)$ uses Bayes' rule and the conditional p.d.f.'s:

$$\mu_i(k) = \frac{p(\mathbf{y}(k) \mid \mathbf{Y_{k-1}}, M_i) p(M_i \mid \mathbf{Y_{k-1}})}{p(\mathbf{y}(k) \mid \mathbf{Y_{k-1}})} = \frac{p(\mathbf{y}(k) \mid \mathbf{Y_{k-1}}, M_i) \mu_i(k-1)}{\sum_{j=1}^{2} p(\mathbf{y}(k) \mid \mathbf{Y_{k-1}}, M_j) \mu_j(k-1)} \tag{12}$$

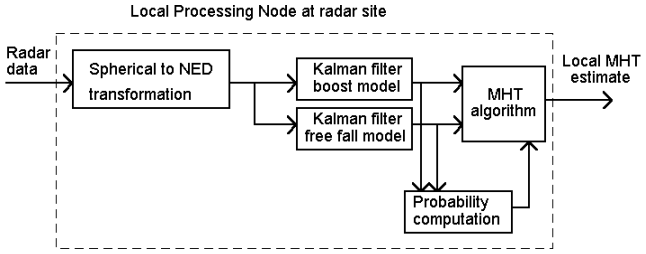

Figure 3 - Multiple hypothesis testing (MHT) structure at each radar site.

The likelihood function $\lambda_j(k)$ is the conditional p.d.f. $p(\mathbf{y}(k) \mid \mathbf{Y_{k-1}}, M_j)$ that observation $\mathbf{y}(k)$ occurs assuming the validity of model M_j. $\lambda_j(k)$ is extracted from the innovation process in the j-th Kalman filter $\mathbf{r_j}(k) = \mathbf{y}(k) - \mathbf{H}\hat{\mathbf{x}}_j(k \mid k-1)$ assuming it is Gaussian, zero mean, and with covariance $\mathbf{S_j}(k \mid k-1) = \mathbf{H}\mathbf{P_j}(k \mid k-1)\mathbf{H}^T + \mathbf{R_{radar,c}}$ as follows:

$$\lambda_j(k) = p(\mathbf{y}(k) \mid \mathbf{Y_{k-1}}, M_j) = \frac{1}{(2\pi)^{m/2} \left|\mathbf{S_j}\right|^{1/2}} \exp\left(-\frac{1}{2}\mathbf{r_j}^T \mathbf{S_j}^{-1} \mathbf{r_j}\right) \tag{13}$$

From equations (12) and (13), the probability $\mu_i(k)$ that a given model M_i is correct is updated by means of:

$$\mu_i(k) = \frac{\lambda_i(k)\mu_i(k-1)}{\sum_{j=1}^{2} \lambda_j(k)\mu_j(k-1)} \tag{14}$$

The output of the MHT structure is the estimate $\hat{\mathbf{z}}_{\mathbf{MHT}}$ of the variable of interest $\mathbf{z}$, which may be a subset of the state $\mathbf{x}$. The MHT estimate $\hat{\mathbf{z}}_{\mathbf{MHT}}(k \mid k)$ is the weighed average of the variable of interest $\hat{\mathbf{z}}_{\mathbf{j}}(k \mid k)$ computed in the j-th filter, j=1,2 considering their respective probabilities in Eq. (14) (Bar-Shalom and Fortman, 1988). Hence:

$$\hat{\mathbf{z}}_{\mathbf{MHT}}(k \mid k) = E\{\mathbf{z}(k) \mid \mathbf{Y_k}\} = \sum_{j=1}^{2} \hat{\mathbf{z}}_{\mathbf{j}}(k \mid k) p(M_j \mid \mathbf{Y_k}) = \sum_{j=1}^{2} \hat{\mathbf{z}}_{\mathbf{j}}(k \mid k) \mu_j(k) \tag{15}$$

The corresponding MHT error covariance is:

$$\mathbf{P}_{\mathbf{MHT},\hat{z}\hat{z}}(k \mid k) = \sum_{j=1}^{2} \mu_j(k)(\mathbf{P}_{\mathbf{j},\hat{z}\hat{z}}(k \mid k) + (\hat{\mathbf{z}}_{\mathbf{j}}(k \mid k) - \hat{\mathbf{z}}_{\mathbf{MHT}}(k \mid k))(\hat{\mathbf{z}}_{\mathbf{j}}(k \mid k) - \hat{\mathbf{z}}_{\mathbf{MHT}}(k \mid k))^T) \tag{16}$$

Initial probabilities were 99.9% for boosted flight, and 0.01% for free fall. A lower bound on computed probabilities has been set to 10^{-8} in Eq. (14). Probabilities μ_j j=1,2 have been most of the time at their extreme values and the transitions occurred nearly as a switch. However, low quality measurements caused transitions that not always reflected the actual flight phase. Occasionally, the transition between models was not complete long after an actual flight phase shift has occurred. In such cases, anomalous fluctuations were observed in $\mathbf{P_{MHT}}$. The latter in Eq. (16) is related to the probabilistic model weighing in Eq. (14). Correct CI-based fusion requires that $\mathbf{P_{MHT}}$ should not be affected by those artifacts. Divergence is avoided by accurate, fast switching between models. Therefore, model probabilities μ_j j=1,2 in Eq. (14) are modified for use in Eqs. (15)-(16) according to the following *ad-hoc* modification:

$$\mu_1^*(k) = \begin{cases} 1 \text{ if } \mu_1(k) > 1/2 \\ 0 \quad \text{otherwise} \end{cases} \qquad \mu_2^*(k) = 1 - \mu_1^*(k) \tag{17}$$

4. Covariance intersection (CI) fusion

The fusion process exploits the complementary characteristics of both radar sites, Adour and Atlas for short and long range, respectively. Covariance intersection (CI) is an adequate approach for sensor fusion when there is no knowledge of sensor cross-correlation that arise from the radars tracking the same target (Peters, 2001; Uhlmann *et al.*, 1997). Often correlations are ignored and information sources are assumed to be independent, which may cause divergence when the computed covariance matrix underestimates the actual estimation errors.

Consider two pieces of information, A and B, which come from different sources and must be fused in order to achieve an output C. A and B are corrupted by noise, and they are modelled as random variables **A** and **B** with unknown true statistics. Available are consistent estimates of their means and covariances, respectively, $\{\mathbf{a},\mathbf{P}_{aa}\}$ and $\{\mathbf{b},\mathbf{P}_{bb}\}$ according to the standard definition of consistency (Jazwinsky, 1970; Uhlmann *et al.*, 1997). The deviations $\tilde{\mathbf{a}}$ and $\tilde{\mathbf{b}}$ about the unknown true means $\bar{\mathbf{a}}$ and $\bar{\mathbf{b}}$, respectively, are defined as $\tilde{\mathbf{a}} = \mathbf{a} - \bar{\mathbf{a}}$ and $\tilde{\mathbf{b}} = \mathbf{b} - \bar{\mathbf{b}}$. The deviations have nonzero means, and their mean square errors and cross-correlation are given by $\bar{\mathbf{P}}_{aa} = \mathrm{E}\{\tilde{\mathbf{a}}\tilde{\mathbf{a}}^{\mathrm{T}}\}$, $\bar{\mathbf{P}}_{bb} = \mathrm{E}\{\tilde{\mathbf{b}}\tilde{\mathbf{b}}^{\mathrm{T}}\}$, and $\bar{\mathbf{P}}_{ab} = \mathrm{E}\{\tilde{\mathbf{a}}\tilde{\mathbf{b}}^{\mathrm{T}}\}$. Even when the actual values are not known, the local estimates $\mathbf{P}_{aa}$ and $\mathbf{P}_{bb}$ are consistent if $\mathbf{P}_{aa} - \bar{\mathbf{P}}_{aa} \geq \mathbf{0}$ and $\mathbf{P}_{bb} - \bar{\mathbf{P}}_{bb} \geq \mathbf{0}$.

The cross-correlation $\bar{\mathbf{P}}_{ab}$ is not known and, generally, is nonzero. The fusion of information from A and B provides the output C, which consists of the estimates of the mean and covariance $\{\mathbf{c},\mathbf{P}_{cc}\}$, respectively, that minimizes some cost function and guarantees consistency. The latter is given by $\mathbf{P}_{cc} - \bar{\mathbf{P}}_{cc} \geq \mathbf{0}$, $\bar{\mathbf{P}}_{cc} = \mathrm{E}\{\tilde{\mathbf{c}}\tilde{\mathbf{c}}^{\mathrm{T}}\}$, where $\tilde{\mathbf{c}} = \mathbf{c} - \bar{\mathbf{c}}$, and $\bar{\mathbf{c}}$ is the true mean. Myriad fusion methods compute a linear combination of the estimates **a** and **b**, and analytically determine the covariance of the result. This leads to an optimal result when knowledge is available about the actual system statistics. Often, however, even the extensive use of empirical information is not enough to achieve that knowledge due to uncertainty in the cross-correlation. The Kalman Filter, for instance, linearly combines estimates $\{\mathbf{a},\mathbf{P}_{aa}\}$ and $\{\mathbf{b},\mathbf{P}_{bb}\}$ into the fused estimates $\{\mathbf{c},\mathbf{P}_{cc}\}$ according to:

$$\mathbf{c} = \mathbf{W}_a\mathbf{a} + \mathbf{W}_b\mathbf{b} \qquad \mathbf{P}_{cc} = \mathbf{W}_a\mathbf{P}_{aa}\mathbf{W}_a^{\mathrm{T}} + \mathbf{W}_a\mathbf{P}_{ab}\mathbf{W}_b^{\mathrm{T}} + \mathbf{W}_b\mathbf{P}_{ba}\mathbf{W}_a^{\mathrm{T}} + \mathbf{W}_b\mathbf{P}_{bb}\mathbf{W}_b^{\mathrm{T}} \tag{18}$$

Weights $\mathbf{W}_a$ and $\mathbf{W}_b$ minimize the trace of $\mathbf{P}_{cc}$. Equation (18) yields the fusion covariance estimate $\mathbf{P}_{cc}$ based on the covariances estimates $\mathbf{P}_{aa}, \mathbf{P}_{ab}, \mathbf{P}_{bb}$. However, the true fusion covariance $\bar{\mathbf{P}}_{cc}$ is:

$$\bar{\mathbf{P}}_{cc} = \mathbf{W}_a\bar{\mathbf{P}}_{aa}\mathbf{W}_a^{\mathrm{T}} + \mathbf{W}_a\bar{\mathbf{P}}_{ab}\mathbf{W}_b^{\mathrm{T}} + \mathbf{W}_b\bar{\mathbf{P}}_{ba}\mathbf{W}_a^{\mathrm{T}} + \mathbf{W}_b\bar{\mathbf{P}}_{bb}\mathbf{W}_b^{\mathrm{T}} \tag{19}$$

Consistency of estimates $\{\mathbf{a},\mathbf{P}_{aa}\}$ and $\{\mathbf{b},\mathbf{P}_{bb}\}$ is enough to ensure consistency in Eq. (18) when $\mathbf{P}_{ab} = \bar{\mathbf{P}}_{ab} = \mathbf{0}$ (Jazwinski, 1970). Consistency in Eq. (18) is not assured when the actual correlation $\bar{\mathbf{P}}_{ab} \neq \mathbf{0}$. Fortunately, CI circumvents the need for knowledge of the cross-correlation. CI can be underconfident, as Peters (2001) points out that its output is never more confident than the most confident of its inputs. He claims that such quality ensures that no degree of cross-correlation among local-level processing nodes will cause filter divergence, which is a most valuable feature. CI applies a convex combination of means and covariances in the inverse covariance space (Uhlmann *et al.*, 1997). The intuition behind CI can be understood from a 2-D geometric interpretation of Eq. (18). Let a 1-sigma 2-D covariance ellipse be the locus of points $\{\mathbf{p}: \mathbf{p}^{\mathrm{T}}\mathbf{P}^{-1}\mathbf{p}=\text{constant}\}$. Plotting the covariance ellipses of $\mathbf{P}_{aa}$, $\mathbf{P}_{bb}$, and $\mathbf{P}_{cc}$ for many choices of $\mathbf{P}_{ab}$ makes clear the fact that $\mathbf{P}_{cc}$ always lies within the intersection region of $\mathbf{P}_{aa}$ and $\mathbf{P}_{bb}$. The Kalman-based fusion update, which assumes independent sources $\mathbf{P}_{ab} = \mathbf{0}$, yields a $\mathbf{P}_{cc}$-ellipse inside the intersection region. This Kalman-ellipse represents the overconfidence of Kalman-fused estimates in comparison with other $\mathbf{P}_{cc}$-ellipses that lie inside the intersection region, and result from some choice of $\mathbf{P}_{ab} \neq \mathbf{0}$, and are not enclosed by the Kalman-ellipse. Extending to more dimensions than the previous 2-D analogy, if a $\mathbf{P}_{cc}$-ellipsoid is found that encloses the intersection region of $\mathbf{P}_{aa}$ and $\mathbf{P}_{bb}$ for any possible choice of $\mathbf{P}_{ab}$, then one can say that the estimates are consistent even if there is no knowledge about $\mathbf{P}_{ab}$. Graphically, the tighter the ellipsoid encloses the intersection region, the more effective is the use of the available information for fusion. The CI-based fusion covariance equation for two information sources is:

$$\mathbf{P}_{cc}^{-1} = \omega\mathbf{P}_{aa}^{-1} + (1-\omega)\mathbf{P}_{bb}^{-1}, \ \omega \in [0,1] \tag{20}$$

The above fusion is consistent for all choices of $\mathbf{P}_{ab}$ and ω (Uhlmann,1997). Cost functions which are convex with respect to ω have only one distinct optimum in the range [0,1]. Parameter ω minimizes the determinant of $\mathbf{P}_{cc}$, and must be continuously recomputed since a constant ω might cause filter divergence. Once the optimal ω has been computed, the fused estimate is obtained from $\mathbf{P}_{cc}^{-1}\mathbf{c} = \omega\mathbf{P}_{aa}^{-1}\mathbf{a} + (1-\omega)\mathbf{P}_{bb}^{-1}\mathbf{b}$. The flowchart diagram in Figure 4 shows the information flow from radar sites to local-level processing nodes to CI-based fusion:

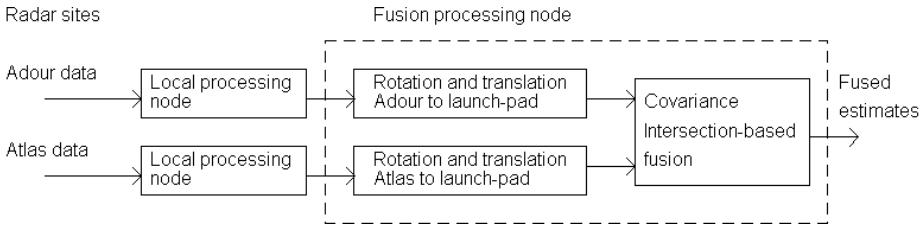

Figure 4 - The CI-based fusion system

5. Impact point prediction (IPP) and its uncertainty area

The impact point is the touchdown location on the surface of the spherical Earth (radius R_{ti}) under the assumption of ballistic flight following an instantaneous ending of propulsion. Fused position and velocity estimates $\mathbf{R_k}$ and $\mathbf{V_k}$ are in the ENU (East-North-Up) coordinate frame. IPP estimates are computed in the Earth-centered Earth-fixed (ECEF) coordinate frame because gravity is naturally represented in that reference frame. Hence, the Z_E-axis is along the direction of rotation of the Earth, X_E along the intersection of the plane of the Greenwich meridian with the Earth's equatorial plane, and Y_E completes the triad. A transformation of fused position and velocity estimates from ENU to ECEF is carried out. The geometry of the free-fall trajectory is governed by the Keplerian laws of orbital motion in polar coordinates of the trajectory plane defined by $\mathbf{R_k}$ and $\mathbf{V_k}$.

Not shown here for lack of space, the IPP equations with $\mathbf{R_k}$ and $\mathbf{V_k}$ *represented in ECEF coordinates* demand the continuous estimation of the semi-major axis of the elliptical free-fall trajectory, its eccentricity, and the excentric and true anomalies. The IPP equations yield the nominal impact point latitude, longitude, and time-to-impact. IPP uncertainty is derived from information about position and velocity estimation errors embedded in the covariance matrix $\mathbf{P_{cc}}$, and leads to the computation of an uncertainty area on the ground with a given probability of impact.

Position error uncertainty in the 3D space can be represented by a covariance ellipsoid portraying a desired bound on the probability of occurrence (Woodburn and Tanygin, 2002). The same applies to representations of fused velocity and acceleration. The eigenvalue-eigenvector decomposition of $\mathbf{P_{cc}}$ provides the information about the principal directions and respective sizes of the uncertainty ellipsoid in ECEF coordinates. The 9-D covariance ellipsoid from $\mathbf{P_{cc}}$ is given by the locus $\{\mathbf{p}: \mathbf{p}^T\mathbf{P_{cc}}^{-1}\mathbf{p}=\text{constant}\}$. Reduction from the coupled 9-D covariance space to position, velocity, and acceleration uncertainties in the 3-D physical space is performed via inversion of the full 9-D covariance matrix and extraction of the 3x3 blocks of interest (Woodburn and Tanygin, 2002). The inversion of the full 9x9 $\mathbf{P_{cc}}$ keeps the information about cross-correlation embedded in the 3x3 blocks of interest.

Position and velocity uncertainty ellipsoids are obtained from the eigenvalues and eigenvectors of the corresponding 3x3 sub-matrices. The eigenvectors provide the orientation of the 3D ellipsoid principal axes relative to the ECEF reference system. For instance, the region enclosed by the position uncertainty ellipsoid with one-sigma size implies a $P_{3D}(1)=19.87\%$ probability of containing the sounding rocket (Woodburn and Tanygin, 2002). Different probability levels $P_{3D}(k)$ relate to standard-deviation units of length *k* along the ellipsoid principal axes.

The influence of position uncertainty on impact area prediction was seen to be negligible. Notice that in a different data set, in which velocity estimates present small errors, applying such a simplification demands caution. The prediction of an area on the ground with a given probability of impact is straightforward when neglecting position uncertainty since the only source of uncertainty is the velocity ellipsoid sized according to that probability. The probability of an impact occurring inside the impact area on the ground is the same as that of the actual velocity vector lying inside its uncertainty ellipsoid about the fused estimate. Thus, fused position and velocity estimates $\mathbf{R_k}$ and $\mathbf{V_k}$, respectively, and the grid approximating the latter's ellipsoid of uncertainty with a given probability are continuously mapped on the corresponding impact area on the ground by means of the IPP equations.

6. Results

Information from Atlas is significantly incorrect in the initial moments because that radar site has no direct line-of-sight to the target at the launch pad. Results not shown here clearly indicate the prevalence of information derived from short range Adour data in the initial boost stage, followed by long range Atlas data prevailing along the rest of the trajectory. The fused solution is robust to the noisy output of the processing node dealing with data from Adour, which is a proximity radar dedicated to tracking lift-off and the first moments of the boosted phase. *Contrary to the present procedure at Alcântara Launch Center, CI-based fusion weighs the proximity radar Adour and long range Atlas without interference of the expert safety-of-flight officer, and automatically reproduces the expert's considerations.*

Figure 5 shows acceleration (top set of strip charts) and velocity estimates along the launch-pad North, East, and Up directions from both processing nodes, Adour and Atlas, and the results of fusing them during boosted flight and free fall up to 50s. The fused estimates are not affected neither by the diverging Atlas's estimates at close range or Adour's divergence at long range. The vertical channel acceleration in Fig. 5 indicates the transition from boost to free fall occurring between 20s and 25s.

Figure 6 on the left shows a snapshot of the uncertainty area on the ground surrounding the nominal impact point and the fused trajectory estimate. A map of the Alcântara peninsula is superimposed on the local horizontal plane at the launch-pad. Each radar-to-target line-of-sight appears in red, and the fused trajectory estimate in green. Adour is the radar nearest to the launch-pad. Contrary to the existing procedures in ALC that often yield a poor-quality impact point, the predicted impact area on the ground remains mostly stationary during free fall, changing its size and orientation in response to the time-varying uncertainties and changing radar-to-target line-of-sight geometry. The figure on the right presents the uncertainty ellipsoids magnified by different factors aiming at a better visualization. Actual impact was within two to three hundred meters from the final estimate.

7. Conclusion

This work proposed a fusion approach for the tracking of sounding rockets and impact point prediction during launch operations at the Alcântara Launch Center. Multiple models based on previous work by Singer (1970) used at local-level Kalman filters provide flexibility concerning the adequacy of target models. Modularity has been applied to the approach, as distinct models can be used in a straightforward manner to describe target maneuverability in other applications. Video animations of the results are found in http://www.ele.ita.br/sitdl.

Convergence and conservative error estimation in the face of cross-correlated data sources make Covariance Intersection-based fusion a suitable choice for distributed sensors tracking the same target. A comparative performance evaluation of Covariance Intersection (CI) against measurement fusion and track-to-track fusion is now under way. The CI-based fusion system should be further investigated and validated with distinct scenarios, target vehicles, sensors, and architectures for distributed processing. Concerning implementation aspects, the addition of other sensors demands few changes whereas system design concepts will be kept untouched. Further development and deployment for real-time operation is feasible with commercial, off-the shelf (COTS) standard hardware resources.

8. Acknowledgements

The authors thank EMBRAER and Fundação Casimiro Montenegro Filho, grant 94/2002-ITA “Control Systems for Aerospace Applications” for the support provided to this research work.

9. References

Bak, T., 2000, “Lecture Notes – Estimation and Sensor Information Fusion. Aalborg University”, Department of Control Engineering, Aalborg, Denmark.

Bar-Shalom, Y., and Li, X., 1993, Estimation and Tracking: Principles, Techniques, and Software, Artech House.

Bar-Shalom, Y. and Fortmann, T. E., 1988, Tracking and Data Association, The Academic Press.

Brookner, E., 1998, Tracking and Kalman Filtering Made Easy, Wiley, New York.

Farina, A. and Grazzini, M., 2002, “Radar Fusion to Detect Targets - Part 2”, Signal Processing, Vol.82, pp. 1096-1108

Jazwinski, 1970, Stochastic Processes and Filtering Theory, The Academic Press.

Lerro, D., and Bar-Shalom, Y., 1993, “Tracking with Debiased Consistent Converted Measurements Versus EKF”, IEEE Transactions on Aerospace and Electronic Systems, Vol.29, No.3, pp. 1015:1022.

Montenbruck, O., Markgraf, M., Jung, W., Bull, B., and Engler, W., 2002, “GPS based prediction of the instantaneous impact point for sounding rockets”, Aerospace Science and Technology, Vol.6, pp. 283-294.

Peters, D. J., 2001, “A Practical Guide to Level One Data Fusion Algorithms”, Defense R&D Canada, Technical Memorandum DREA TM 2001-201.

Rogers, R.M., 2003, Applied Mathematics in Integrated Navigation Systems. Second edition, AIAA.

Singer, R. A., 1970, “Estimating optimal tracking filter performance for manned maneuvering targets”, IEEE Transactions on Aerospace and Electronic Systems, Vol.6, No.4, pp. 473-483.

Uhlmann, J.K., Julier, S.J., Csorba, M., and Durrant-Whyte, H.F., 1997, “A Culminating Advance in the Theory and Practice of Data Fusion, Filtering, and Decentralized Estimation”, Technical Report, Covariance Intersection Working Group (CWIG). http://www.ait.nrl.navy.mil/people/uhlmann/CovInt.html (or at http://citeseer.ist.psu.edu/cache/papers/cs/3620/http:zSzzSzwww.ait.nrl.navy.milzSzpeoplezSzuhlmannzSzCIWG-1.0.pdf/ciwg97culminating.pdf).

Wertz, J.R., 1978, Summary of orbit properties and terminology, In Spacecraft Attitude Determination and Control, page 52, J.R.Wertz (Ed.), Kluwer.

Willsky, A.S., Chow, E.Y., Gershwin, S.B., Greene, C.S., Houpt, P.K., and Kurkjan, A.L., 1980, “Dynamic model-based techniques for the detection of incidents on freeways”, IEEE Transactions on Automatic Control, Vol.25, No.3, pp. 347-360.

Woodburn, J. and Tanygin, S., 2002, “Position Covariance Visualization”, AIAA paper 2002-4985, AIAA/AAS Astrodynamics Specialist Conference and Exhibit, Monterey, CA, USA.

6. Responsibility notice

The authors are the only responsible for the printed material included in this paper.

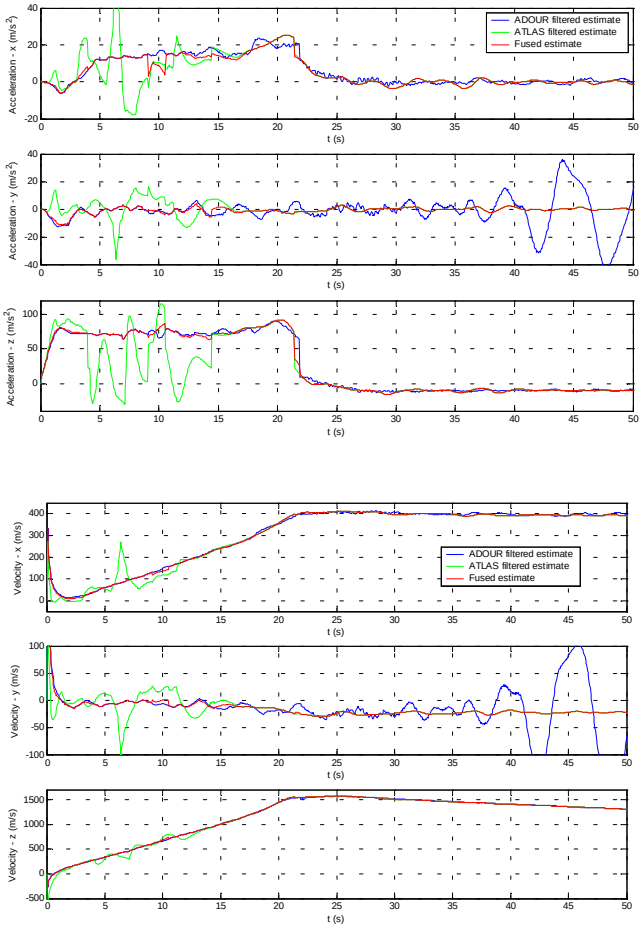

Figure 5 - Acceleration (top) and velocity (down) estimates. Strip charts depict North, East, and vertical Up directions at the launch-pad from the top down, respectively. Color key: Adour (blue), Atlas (green), and fusion (red).

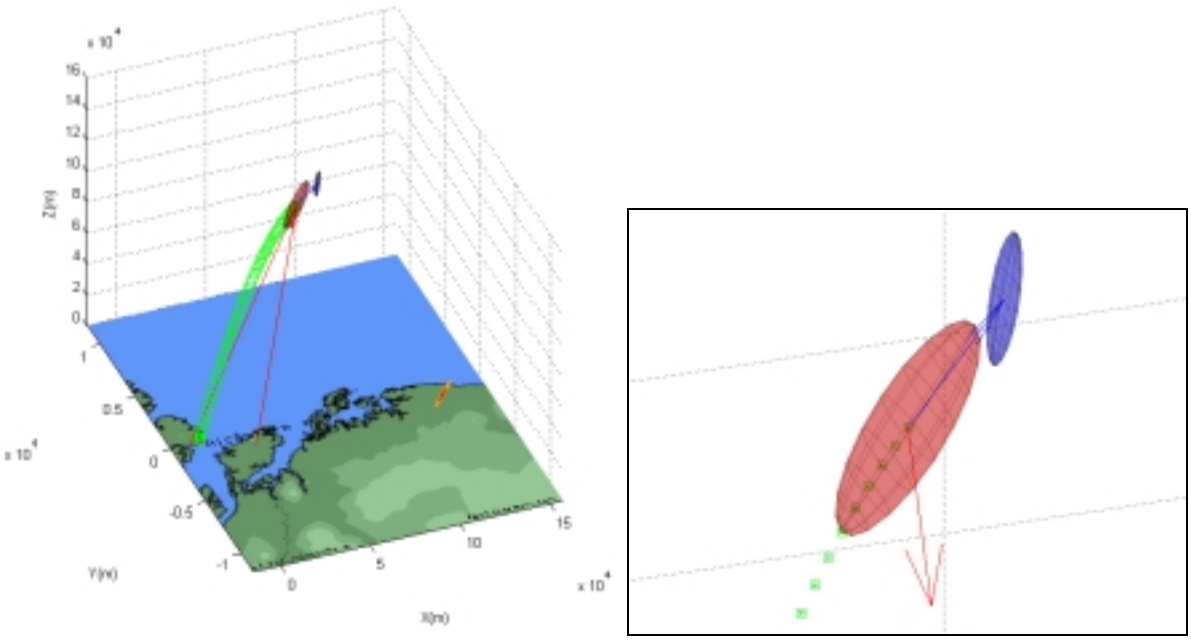

Figure 6 - Left: Fused estimate of the trajectory, covariance ellipsoids and the computed impact area. Ground impact probability levels are 0.1 (red), 0.5 (orange), and 0.95 (yellow). Right: nominal position (green), and position (red) and velocity (blue) covariance ellipsoids with fused acceleration (red) and velocity (blue) estimates.